Available online at www.sciencedirect.com
ScienceDirect
Journal of Power Sources 163 (2006) 450–459
JOURNAL OF POWER SOURCES
www.elsevier.com/locate/jpowsour

Thermal-fluid transports in a five-layer membrane-electrode assembly of a PEM fuel cell

J.J. Hwang [a,*], C.H. Chao [b], W. Wu [c]

[a] *Department of Environment Energy, National University of Tainan, Tainan 700, Taiwan*
[b] *Department of Electrical Engineering, Ta-Hua Institute of Technology, Hsinchu County 307, Taiwan*
[c] *Department of Chemical Engineering, National Yunlin University of Science & Technology, Taiwan*

Received 29 July 2006; received in revised form 18 August 2006; accepted 15 September 2006
Available online 30 October 2006

Abstract

Thermal-fluid transport phenomena in a membrane-electrode assembly (MEA) of a polymer electrolyte membrane (PEM) fuel cell attached to interdigitated gas distributors are studied numerically. The MEA consists of two porous catalyst layers, two porous gas diffusion layers, and an impermeable PEM. In the catalyst layers, the overpotential heating by the electrochemical reaction under thermal equilibrium conditions produces heat that is removed by the fluids as well as the solid matrices. In the diffusion layers, the difference in the heat conductivities between the solid matrices and the fluids causes a thermal non-equilibrium in the porous medium. A two-equation approach is used to resolve the temperature difference between the solid matrices and the fluids. The effects of the porous Reynolds number, interfacial heat transfer coefficient, and overpotential heating are examined. It is found that the local maximum temperature occurs inside the cathodic catalyst layer. In addition, the temperature difference between the solid matrices and the fluids in the diffusion layers decreases with increasing the non-dimensional interfacial heat transfer coefficient. The present results have provided comprehensive heat transfer information that is helpful in understanding of the mechanisms responsible for thermal pathways in a PEM fuel cell.

Keywords: PEM fuel cells; Membrane-electrode assembly (MEA); Gas diffusion layer; Catalyst layer

1. Introduction

Fuel cells convert directly the chemical energy of fuels to electricity through electrochemical reactions. The combination of benefits in high efficiency, eco-friendly nature, and diversity in fuels makes them attractive alternative power conversion devices. The classification of fuel cells is commonly based on the electrolyte material, including polymer electrolyte membrane (PEMFC), solid oxide (SOFC), molten carbonate (MCFC), potassium hydroxide (AFC), and phosphoric acid (PAFC). Among them, PEM fuel cells have appeared as the most promising candidates for commercial applications.

To improve the understanding of the characteristics in a PEM fuel cell, a large amount of experimental efforts have been devoted in the past decade. Common techniques include the ac-impedance approach that determines the impedance characteristics and accesses the modes of failure of a PEM fuel cell, and the polarization-curve measurement that provides the operating *I–V* data of a PEM fuel cell. In general, these experiments provide overall information but lack for revealing detailed characteristics inside a PEM fuel cell such as local temperature distributions. It is known that the efficiency and durability of a PEM fuel cell are strongly affected by the temperature distributions inside the fuel cell. The present instruments cannot support such measurements due to the highly reactive environment and compactness of a fuel cell. Thus, thermal-fluid transport phenomena in the PEM fuel cell are still not well understood. Such information should be sought relying on modeling or simulation.

A large amount of fuel cell models have been developed accounting for various physical processes. Due to space limitation, only some relevant works are briefly reviewed below. Bernardi and Verbrugge [1] proposed a one-dimensional computational model to address the water management and species transport in the cathodic gas channel and gas diffusion layer attached to the membrane. Assumptions used in this model are isothermal, steady state, and ideal gases. Springer et al. [2] pre-

* Corresponding author. Tel.: +886 62600321; fax: +886 422518272.
E-mail address: azaijj@nutn.edu.tw (J.J. Hwang).

0378-7753/$ – see front matter © 2006 Elsevier B.V. All rights reserved.
doi:10.1016/j.jpowsour.2006.09.032

Nomenclature

Bi	Biot number, Table 2
c_{H_2O}	water vapor mole concentration (mol m^{-3})
$c_{H_2O,\,ref}$	water vapor mole concentration at inlet (mol m^{-3})
C_{H_2O}	normalized water vapor concentration, Table 2
$C_{H_2O,\,ref}$	normalized water vapor mole concentration at inlet, Table 2
c_{O_2}	oxygen concentration (mol m^{-3})
$c_{O_2,ref}$	oxygen mole concentration at inlet (mol m^{-3})
C_{O_2}	normalized oxygen concentration, Table 2
$C_{O_2,ref}$	normalized oxygen mole concentration at inlet, Table 2
c_p	specific heat at constant temperature (J kg^{-1} K^{-1})
c_{tot}	total mole concentration of the reacting fluid (mol m^{-3})
d	pore diameter of the porous medium (m)
D_{H_2}	hydrogen diffusivity (m^2 s^{-1})
$D_{H_2,eff}$	effective diffusivity of hydrogen (m^2 s^{-1})
D_{O_2}	diffusivity of oxygen (m^2 s^{-1})
$D_{O_2,eff}$	effective diffusivity of oxygen (m^2 s^{-1})
Da	Darcy number, Table 2
Ec_{O_2}, Ec_{H_2}, Ec_{H_2O}	non-dimensional electrochemical-reaction heating, Table 2
F	Faraday's constant (96487 C mol^{-1})
h_v	interstitial heat transfer coefficient (W m^{-3} K^{-1})
j_o	exchange current density (A m^{-3})
j_T	transfer current density (A m^{-3})
k	thermal conductivity (W m^{-1} K^{-1})
Mt_{O_2}, Mt_{H_2}, Mt_{H_2O}	non-dimensional mass transfer coefficient, Table 2
p	pressure (Pa)
P	non-dimensional pressure, Table 2
Pr	Prandtl number, Table 2
R_k	ratio of fluid-to-solid conductivity, Table 2
Re	Reynolds number, Table 2
S_e	source term for the energy equation
S_i	source term for the concentration equation
S_m	source term for the momentum equation
Sc	Schmidt number, Table 2
T	temperature (K)
$\mathbf{u}$, $\mathbf{U}$	velocity vectors
u_d	pore velocity in the porous medium (m s^{-1})
U, V	non-dimensional velocity components in the X, and Y direction
W	witdth of the computational domain (m)
X, Y	coordinate system, Fig. 2

Greek letters

α_1, α_2	coefficients in Eq. (9)
β_1	coefficient in Eq. (8)
δ	thickness of the five-layer MEA (m)
ε	porosity
η	overpotential (V)
κ	permeability (m^2)
θ	non-dimensional temperature, Table 2
ρ	density (kg m^{-3})
τ	tortuosity of the porous electrode

Subscripts

a	anode
c	cathode or catalyst layer
CL	catalyst layer
d	diffusion layer
eff	effective
f	fluid phase
HOR	hydrogen oxidation reaction
i	species
m	membrane
ORR	oxygen reduction reaction
ref	reference
s	solid phase
tot	total

sented an isothermal, one-dimensional, steady state model for a PEM fuel cell with a hydrated Nafion-117 membrane. The unique feature of this model is the empirical relation for calculating membrane conductivity based on water content in the membrane. Nguyen and White [3] presented a steady state, two-dimensional mass transfer model. The model domain consists of gas flow channels, gas diffusion layers, catalyst layers, and membrane. Gurau et al. [4] applied computational fluid dynamics to fuel cell modeling where they began with a two-dimensional model consisting of both the anode and cathode sides. This model fully accounted for the mass transport of reactant species which have been simplified in earlier models. Yi and Nguyen [5] modified their previous model to include heat and mass transfer conditions in both the liquid and gas phases along the flow path of the fuel cell. Shimpalee and Dutta [6] described a steady state, isothermal, three-dimensional, and single phase PEM fuel cell model. A commercial code was used to solve the complete Navier–Stokes equations. Hwang et al. [7–9] described a non-isothermal model for the cathodic half-cell of a PEM fuel cell. Non-dimensional forms of the governing equations were developed and the effects of dimensionless parameters on fuel cell performance were evaluated.

From the above discussion, it is obvious that most previous fuel cell models regarded the electrochemical reaction as an isothermal process. Studies of thermal-fluid transports in the PEM fuel cells are rather sparse. The present study extends the authors' previous work of cathodic heat transfer [7–9] to study the heat/mass transfer in an entire membrane-electrode assembly of a PEM fuel cell. A computational model considering local thermal non-equilibrium (LTNE) in the gas diffusion layers are developed to study the detailed thermal-fluid behaviors in a PEM fuel cell. Although, the LTNE analysis of heat transfer in the porous medium is not new [10–14], a systematical study on the LTNE characteristics of a five-layer membrane-electrode assembly of a PEM fuel cell that is coupled with the electrochemical reaction might be considered to be original and valuable.

2. Numerical model

2.1. Model descriptions

A typical PEM fuel cell with interdigitated gas distributors is schematically shown in Fig. 1. The computational domain is confined within a five-layer membrane-electrode assembly (MEA), i.e., two gas diffusion layers (GDL), two catalyst layers (CL), and a polymer electrolyte membrane (PEM). Electrochemical reactions in the MEA include the hydrogen oxidation reaction (HOR) in the anodic catalyst layer and the oxygen reduction reaction (ORR) in the cathodic catalyst layer. The hydrogen enters the anode from the bottom-left corner of the module, traverses the anodic diffusion layer to the anodic catalyst layer, and is consumed by HOR. Meanwhile, the protons and heat are produced in the anodic catalyst layer, i.e.,

$$\tfrac{1}{2}H_2 \rightarrow H^+ + e^- + \text{Heat} \quad (1)$$

The un-reacted hydrogen exits by the bottom-right corner of the module. In the cathode, the oxygen enters the cathodic diffusion layer from the upper-left corner of the module, transverses the diffuse layer to the catalyst layer, and then reacts together with the protons to form water and heat.

$$\tfrac{1}{4}O_2 + H^+ + e^- \rightarrow \tfrac{1}{2}H_2O + \text{Heat} \quad (2)$$

Finally, the products (water vapor) exit by the upper-right corner of the module.

Physical and geometric parameters of each layer of the MEA are given in Table 1. The coordinate system of the computational domain is shown in Fig. 2. The assumptions used in this model are as follows [15]:

(1) Gas mixtures are ideal gas.
(2) The fluid flow is steady, laminar, and incompressible; its thermal physical properties are constant.
(3) Porous electrode is homogeneous and isotropic with uniform morphological properties such as porosity, tortuosity and permeability.
(4) Water in the electrode exits as vapor only.
(5) Catalyst layer is treated as an ultra-thin layer; thus the oxygen reduction reaction is considered to occur only at the surfaces of the catalyst layer.
(6) The inlet fluid and rib-surface temperatures are uniform.

Table 1
Physical and geometric parameters of the five-layer MEA

Description	Value
Porosity, ε	
Gas diffusion layer, ε_{GDL}	0.48
Catalyst layer, ε_{CL}	0.42
Permeability, κ (m^2)	
Gas diffusion layer, κ_{GDL}	1.57×10^{-12}
Catalyst layer, κ_{CL}	1.02×10^{-12}
Tortuosity, τ	
Gas diffusion layer, τ_{GDL}	1.5
Catalyst layer, τ_{CL}	1.5
Thermal conductivity, k ($W\,kg^{-1}\,K^{-1}$)	
Gas diffusion layer, $k_{s,eff}$	1.7
PEM, k_m	0.5
Anode gas, $k_{f,eff}$	0.182
Cathode gas, $k_{f,eff}$	0.051
MEA dimensions (μm)	
Gas diffusion layer thickness, δ_{GDL}	200
Catalyst layer thickness, δ_{CL}	25
PEM thickness, δ_m	50
MEA thickness, δ	500

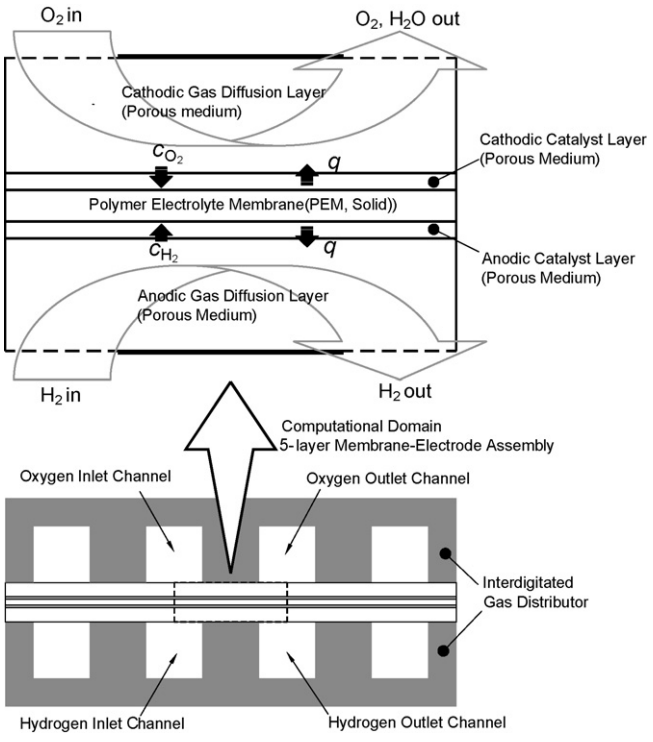

Fig. 1. Schematic drawing of the five-layer MEA of a PEM fuel cell with interdigitated gas distributors.

δ_{GDL}/δ	δ_m/δ	δ_{CL}/δ	W/δ
0.4	0.1	0.05	1.6

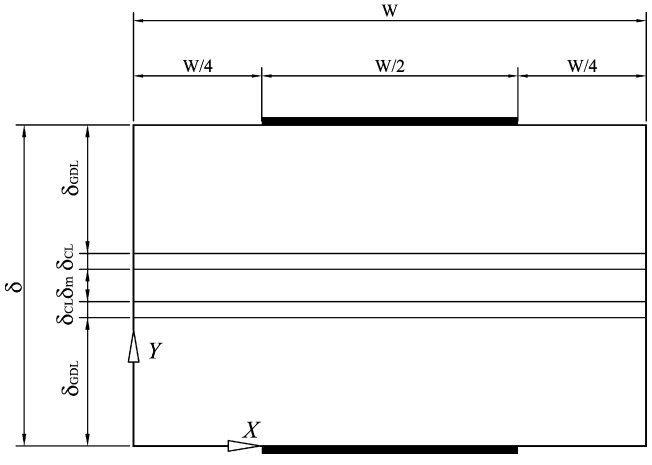

Fig. 2. Dimensions and coordinate system of the computational module.

2.2. Momentum transports

The mass conservation equation together with the Brinkman-extended Darcy equation describes the fluid flow in the gas diffusion layers.

$$\nabla(\rho\mathbf{u}) = 0 \tag{3}$$

$$\rho\mathbf{u}\cdot\nabla\mathbf{u} = -\nabla p + \nabla\cdot(\mu\nabla\mathbf{u}) + S_{\mathrm{m}} \tag{4}$$

The source term in the momentum equations is $S_{\mathrm{m}} = -(\mu/\kappa)\varepsilon\mathbf{u}$, respectively. Using the non-dimensional parameters list in Table 2, the above equations are further reduced to dimensionless forms of:

$$\nabla\mathbf{U} = 0 \tag{5}$$

$$\mathbf{U}\cdot\nabla\mathbf{U} = -\nabla P + \frac{1}{Re}\nabla^2\mathbf{U} - \frac{\varepsilon}{Re\cdot Da}|\mathbf{U}| \tag{6}$$

2.3. Concentration distributions

The species transports in the electrodes are described by the following equations:

$$\mathbf{u}\cdot\nabla c_{\mathrm{i}} = D_{\mathrm{i}}\nabla^2 c_{\mathrm{i}} + S_{\mathrm{i}} \tag{7}$$

The species considered in the anode and cathode are pure hydrogen, $c_{\mathrm{H_2}}$, and the wet oxygen, $c_{\mathrm{O_2}}$ and $c_{\mathrm{H_2O}}$, respectively. The effective diffusivities of the species i in the porous electrode follows the Bruggemann model [16], i.e., $D_{\mathrm{i,eff}} = \varepsilon^{\tau} D_{\mathrm{i}}$. The source term is nothing in the gas diffusion layers. In the catalyst layer, it is implemented based on electrochemical kinetics, i.e., consuming the reactants to produce the current. In the anodic catalyst layer, it becomes $S_{\mathrm{i}} = -(j_{\mathrm{T,HOR}}/2F)$. According to the Butler–Volmer correlation [17], the rate of electrochemical reaction on the reaction surfaces can be described by the relationship of the local current density and the reactant

Table 2
Non-dimensional parameters used in the present study

Symbols	Expression	Physical meanings
Bi	$\dfrac{h_{\mathrm{v}}\delta^2}{k_{\mathrm{s,eff}}}$	Biot number
$C_{\mathrm{H_2}}$, $C_{\mathrm{H_2,ref}}$	$\dfrac{c_{\mathrm{H_2}}}{c_{\mathrm{tot}}}$, $\dfrac{c_{\mathrm{H_2,ref}}}{c_{\mathrm{tot}}}$	Non-dimensional hydrogen concentration
$C_{\mathrm{O_2}}$, $C_{\mathrm{O_2,ref}}$	$\dfrac{c_{\mathrm{O_2}}}{c_{\mathrm{tot}}}$, $\dfrac{c_{\mathrm{O_2,ref}}}{c_{\mathrm{tot}}}$	Non-dimensional oxygen concentration
Da	$\dfrac{\kappa}{\delta^2}$	Darcy number
$\mathrm{Ec_{H_2}}$	$\dfrac{\beta_1\cdot\delta^2\cdot\eta_{\mathrm{a}}}{k_{\mathrm{s,eff}}(T_{\mathrm{f,in}}-T_{\mathrm{r}})C_{\mathrm{H_2,ref}}}$	Ratio of the electrochemical heating to the conduction in solid phase of the anode
$\mathrm{Ec_{H_2O}}$	$\dfrac{\alpha_2\cdot\delta^2\cdot\eta_{\mathrm{c}}}{k_{\mathrm{s,eff}}(T_{\mathrm{f,in}}-T_{\mathrm{r}})C^2_{\mathrm{H_2O,ref}}}$	Ratio of the electrochemical heating to the conduction in solid phase of the cathode
$\mathrm{Ec_{O_2}}$	$\dfrac{\alpha_1\cdot\delta^2\cdot\eta_{\mathrm{c}}}{k_{\mathrm{s,eff}}(T_{\mathrm{f,in}}-T_{\mathrm{r}})C_{\mathrm{O_2,ref}}}$	Ratio of the electrochemical heating to the conduction in solid phase of the cathode
$\mathrm{Mt_{H_2}}$	$\dfrac{j_{\mathrm{o,a}}\cdot\beta_1\cdot\delta^2}{2F\cdot c_{\mathrm{H_2,ref}}\cdot D_{\mathrm{H_2,eff}}}$	Ratio of the hydrogen consumption to the mass diffusion in the anode
$\mathrm{Mt_{H_2O}}$	$\dfrac{j_{\mathrm{o,c}}\cdot\alpha_2\cdot\delta^2}{4F\cdot c_{\mathrm{tot}}\cdot c^2_{\mathrm{H_2O,ref}}\cdot D_{\mathrm{H_2,eff}}}$	Ratio of the hydrogen consumption to the mass diffusion in the anode
$\mathrm{Mt_{O_2}}$	$\dfrac{j_{\mathrm{o,c}}\cdot\alpha_1\cdot\delta^2}{4F\cdot c_{\mathrm{O_2,ref}}\cdot D_{\mathrm{O_2,eff}}}$	Ratio of the oxygen consumption to the mass diffusion in the anode
P	$\dfrac{p}{\rho_{\mathrm{f}}u_{\mathrm{d}}^2}$	Non-dimensional pressure
Pr_{eff}	$\dfrac{\mu(c_p)_{\mathrm{f}}}{k_{\mathrm{f,eff}}}$	Prandtl number
Re	$\dfrac{u_{\mathrm{d}}\delta}{\nu}$	Reynolds number
R_k	$\dfrac{k_{\mathrm{f,eff}}}{k_{\mathrm{s,eff}}}$	Ratio of the fluid-phase conductivity to the solid-phase conductivity
$Sc_{\mathrm{H_2}}$, $Sc_{\mathrm{O_2}}$	$\dfrac{\nu}{D_{\mathrm{H_2,eff}}}$, $\dfrac{\nu}{D_{\mathrm{O_2,eff}}}$	Schmidt numbers for hydrogen and oxygen, respectively
U, V	$U = \dfrac{u}{u_{\mathrm{d}}}$, $V = \dfrac{v}{u_{\mathrm{d}}}$	Non-dimensional velocity
θ	$\dfrac{T-T_{\mathrm{r}}}{T_{\mathrm{f,in}}-T_{\mathrm{r}}}$	Non-dimensional temperature

concentrations, i.e.,

$$j_{T,HOR} = j_{o,a}\beta_1 \left(\frac{c_{H_2}}{c_{H_2,ref}}\right) \tag{8}$$

$$j_{T,OOR} = j_{o,c}\left[\alpha_1\left(\frac{c_{O_2}}{c_{O_2,ref}}\right) - \alpha_2\left(\frac{c_{H_2O}}{c_{H_2O,ref}}\right)^2\right] \tag{9}$$

where $j_{o,a}$ and $j_{o,c}$ are the anodic and cathodic exchange current densities, respectively. α_1, α_2, and β_1 are electrochemical coefficients depending on and the overpotential on the electrode surfaces. All above coefficients are regarded as constants in the present simulation. Based on the non-dimensional parameters in Table 2, the dimensionless forms of the species transport equations in the anodic and cathodic catalyst layers are, respectively, written as

$$\mathbf{U}\cdot\nabla C_{H_2} = \frac{1}{Re\cdot Sc_{H_2}}\nabla^2 C_{H_2} + \frac{Mt_{H_2}}{Re\cdot Sc_{H_2}}C_{H_2} \tag{10}$$

$$\mathbf{U}\cdot\nabla C_{O_2} = \frac{1}{Re\cdot Sc_{O_2}}\nabla^2 C_{O_2} - \frac{1}{Re\cdot Sc_{O_2}}[Mt_{O_2}C_{O_2} - Mt_{H_2O}(1-C_{O_2})^2] \tag{11}$$

2.4. Temperature distributions

In practical applications, the temperature difference between the inlet and the outlet of a PEM fuel cell is not so large, typically about 30–40 K. In addition, the conductivities of the solid matrix (such as carbon fibers) and the reactant fluid (such as air) are quite different. That is the temperature between the solid matrices and the fluids may be different and thus away from the local thermal equilibrium. Therefore, in the present model, a two-equation model is used to describe the thermal behaviors in the gas diffusion layers, i.e.,

$$(\rho c_p)_f \mathbf{u}\cdot\nabla T_f = \nabla\cdot(k_{f,eff}\nabla T_f) - S_{e,GDL} \tag{12}$$

$$0 = \nabla\cdot(k_{s,eff}\nabla T_s) + S_{e,GDL} \tag{13}$$

The source terms in the above equations represent the thermal interaction between the solid matrices and the fluids. They are represented by $S_{e,GDL} = -h_v\cdot(T_s - T_f)$, where h_v is the interfacial heat transfer coefficient (volumetric) between the solid matrices and the reactant fluids in porous medium. Actually, up the present time, the values of h_s for porous electrode has not been determined yet, and thus is not available in the open literature. According to the measured data of the metal foams [11], the typical values of h_v vary from 2.0×10^4 to 2.0×10^5 W m^{-3} K^{-1} for the porosity varying from 0.7 to 0.95. In the present study, the value of h_v for the baseline case ($St = 1.39$) is set to be 1.0×10^6 W m^{-3} K^{-1}. The effective thermal conductivities of the solid phase and the fluid phase are, respectively, defined as

$$k_{s,eff} = (1-\varepsilon)k_s \tag{14}$$

$$k_{f,eff} = \varepsilon k_f \tag{15}$$

where k_s and k_f are the thermal conductivities of the carbon fiber and the reactant fluid, respectively.

In the catalyst layers, the electrochemical reaction for the reactant fluids should take place on the catalyst surfaces under the same temperature (i.e., reacting temperature). Thus, the fluids and the solid matrices should be in thermal equilibrium.

$$T_f = T_s \tag{16}$$

$$(\rho c_p)_f \mathbf{u}\cdot\nabla T_f = \nabla\cdot(k_{CL}\nabla T_f) + S_{e,CL} \tag{17}$$

In the present model, the radiation heat flux and the energy dissipation due to Joule heating are neglected. Therefore, the source term in the catalyst layer is represented by the overpotential heating by the electrochemical activation, i.e., $S_{e,CL} = j_{T,HOR}\times\eta_a$ in the anodic catalyst layer and $S_{e,CL} = j_{T,ORR}\times\eta_c$ in the cathodic catalyst layer, respectively.

The effective thermal conductivity of the catalyst layer is determined by the following equation:

$$k_{CL} = -2k_c + \frac{1}{(\varepsilon/(2k_c+k_f)) + ((1-\varepsilon)/3k_c)} \tag{18}$$

where k_c is the weight-averaged conductivity between the ionic conductor (such as Nafion^{TM}) and the electric conductor (such as Pt/C).

Using the non-dimensional parameters given in Table 2, the dimensionless forms of the energy equations in the diffusion layers for both the anode and the cathode are

$$\mathbf{U}\cdot\nabla\theta_f = \frac{1}{Re\cdot Pr}\nabla^2\theta_f + \frac{Bi}{Re\cdot Pr\cdot R_k}(\theta_s - \theta_f) \tag{19}$$

$$0 = \nabla^2\theta_s - Bi(\theta_s - \theta_f) \tag{20}$$

where Bi is the non-dimensional interfacial heat transfer coefficient (Table 2). In general, it is a function of morphology of the porous matrices. Increasing the surface-to-volume ratio of the porous matrices can enhance h_v that reduced the temperature difference between the solid matrix and the reactant fluid.

In the cathodic and anodic catalyst layers, the dimensionless energy equations become

$$\mathbf{U}\cdot\nabla\theta_f = \frac{1}{Re\cdot Pr}\nabla^2\theta_f + \frac{1}{Re\cdot Pr}[Ec_{O_2}C_{O_2} - Ec_{H_2O}(1-C_{O_2})^2] \tag{21}$$

$$\mathbf{U}\cdot\nabla\theta_f = \frac{1}{Re\cdot Pr}\nabla^2\theta_f + \frac{Ec_{H_2}}{Re\cdot Pr}C_{H_2} \tag{22}$$

In addition, the fluid and the solid have the same temperatures, i.e.,

$$\theta_s = \theta_f \tag{23}$$

As for the PEM, a typical conduction equation is employed to describe the thermal behavior in the impermeable material, i.e.,

$$\nabla\cdot(k_m\nabla T_s) = 0 \tag{24}$$

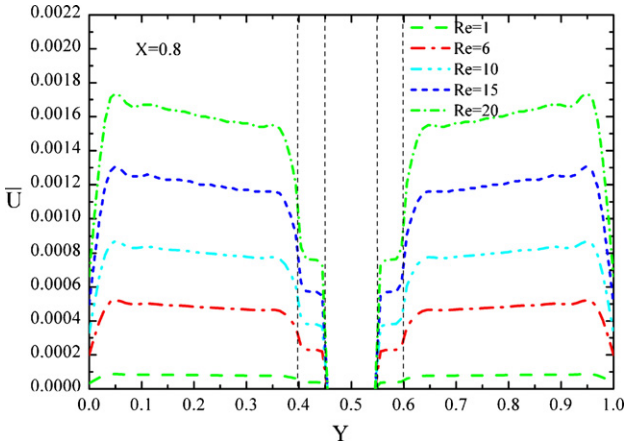

Fig. 3. Effect of Reynolds number on the flow velocity distribution in the MEA.

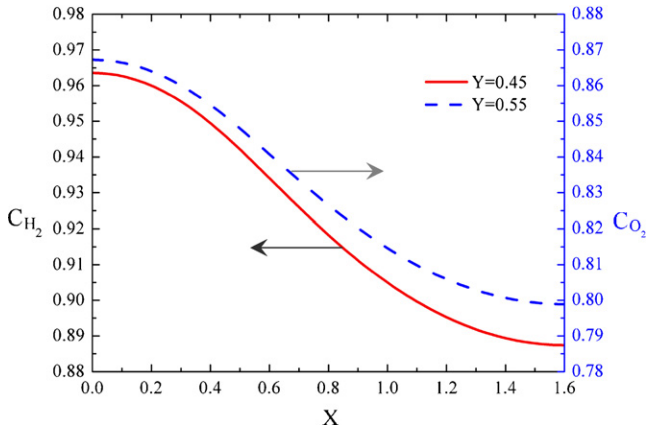

Fig. 5. Distributions of local minimum concentration of hydrogen and oxygen along the flow direction.

where k_m is the ionic conductivity of the PEM. The non-dimensional form of the conduction equation in the PEM becomes

$$\nabla\theta_s^2 = 0 \tag{25}$$

2.5. Boundary conditions

The temperatures for both feeds along with the surfaces of the gas distributor are constant, i.e., $\theta = 1$. Both outlets of the module have a reference (ambient) pressure. The anode is supplied with pure hydrogen, while the cathodic side feeds with the humidified oxygen of 0.9/0.1 for C_{O_2}/C_{H_2O}. Flow rates of the reactants delivered to the cathode and anode are varied by examined the Reynolds number effect ($Re = 1$–20).

2.6. Numerical methods

In the present study, the finite element solutions are obtained with a general purpose commercial solver, COMSOL Multi-physics [18–22]. It uses the Broyden's method with an LU-decomposition pre-conditioner to solve the non-linear equations iteratively. To reduce continuity errors, a penalty term is employed for pressure. Thus, there is a continuous part of the pressure and piecewise constant part providing and extra DOF (degree of freedom) for pressure on each element. It uses Newton–Raphson iteration to solve the close-coupled groups (velocity, pressure, temperature, concentration and electricity) and uses the frontal algorithm (Gaussian elimination) to solve the linearized system of equations for each iteration.

In the present work, all computations are performed on 50×160 ($X \times Y$) structured, orthogonal meshes. Additional runs for the coarser meshes, 40×120, and the finer meshes, 60×180, are taken for a check of grid independence. A comparison of the results of the two grid sizes, 50×160, and 60×180, shows that the maximum discrepancies in the axial velocity and oxygen concentration profiles are only 0.6 and 0.9%, respectively. In addition, results indicate a maximum change of 0.6% in wall temperature distribution between the solutions of 50×160 and

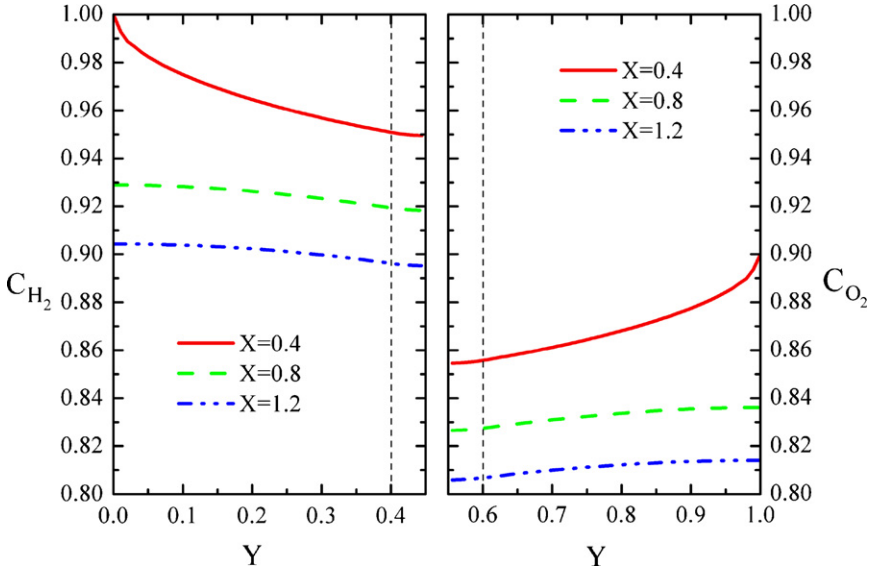

Fig. 4. Species concentration distributions at several axial stations (X) in the MEA.

60×180 grids. All above discrepancies are so small that the accuracy of the solutions on a 50×160 grids is deemed satisfactory. A typical simulation requires about 200 min of central processing unit time on a Pentium IV 2.8 GHz PC.

3. Results and discussion

Before the discussion of the numerical results, it requires to validate the numerical model by comparing the present numerical results with the available experimental data. Up to the present time, it is hard to measure the local temperature inside the porous electrode of a fuel cell. Strictly speaking, no data about the local thermal-fluid characteristics such as local temperatures and heat transfer coefficients inside the porous electrode of a fuel cell are available in the open literature. Therefore, a macroscopic comparison of polarization curve is made between the present predictions and previous experiments [23], which have been widely used to verify a fuel cell simulation model. A comparison of the polarization curve between the present numerical predictions and the experimental data under adiabatic conditions showed a satisfactory agreement.

Fig. 3 shows the flow velocity distribution ($\sqrt{U^2 + V^2}$) at the module middle ($X = 0.8$) as a function of the Reynolds number. The Reynolds number varies from $Re = 1$ to 20. The Darcy numbers are different between the catalyst layer and the gas diffusion layer due to the difference in the permeability. They

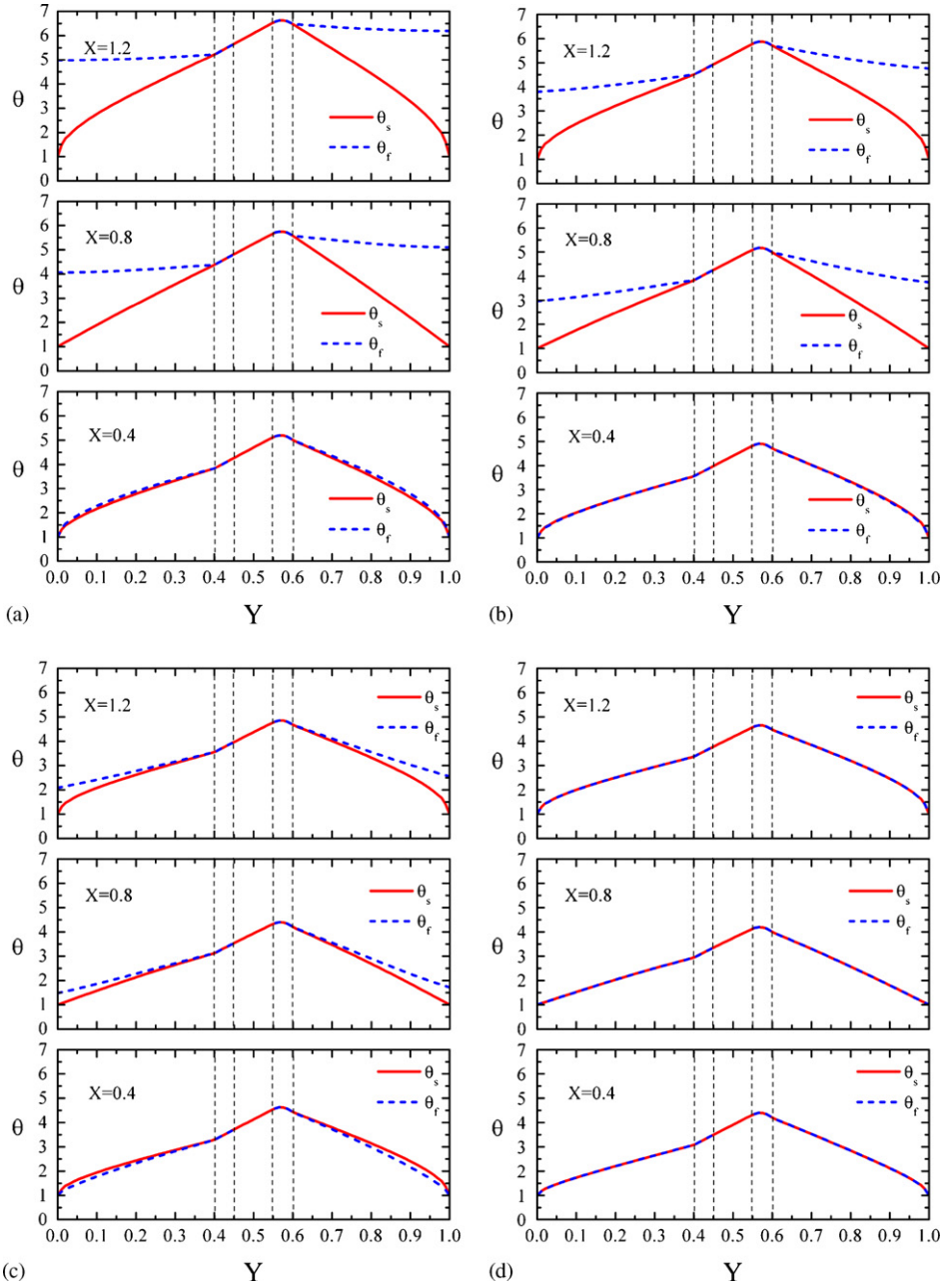

Fig. 6. Comparison of fluid-phase and solid-phase temperature distributions at several X stations in the MEA for (a) $Bi/(Pr{\cdot}Re{\cdot}R_k) = 6.63 \times 10^{-3}$, (b) $Bi/(Pr{\cdot}Re{\cdot}R_k) = 0.663$, (c) $Bi/(Pr{\cdot}Re{\cdot}R_k) = 6.63$, and (d) $Bi/(Pr{\cdot}Re{\cdot}R_k) = 6.63 \times 10^3$.

are $Da = 4.9 \times 10^{-6}$ and $Da = 9.8 \times 10^{-6}$ for the catalyst layers and the gas diffusion layers, respectively. No data are shown in the membrane ($0.45 < Y < 0.55$) since it is impermeable. The gas diffusion layers have a higher permeability and a higher porosity higher than the catalyst layers. Therefore, a higher velocity is accompanied by the gas diffusion layers. In addition, the maximum velocities occur near the shoulder surfaces ($Y = 0$ and 1.0) for the both electrodes. It is reasonable because the pathways from the module inlet to the module outlet are shorter for the flow closer to the shoulder surfaces. A shorter flow pathway pays a smaller pressure-drop penalty, and thus allows more fluids to pass through. It is further seen that the velocity increases with increasing the Reynolds number in both the catalyst layers and the diffusion layers. In addition, the flow velocity distributions show small humps near the interfaces of the catalyst layer and the gas diffusion layer ($Y = 0.4$ and 0.6) and near the rib shoulder ($Y = 0$ and 1.0) due to the shear flows.

Fig. 4 shows the concentration distributions of oxygen (C_{O_2}) and hydrogen (C_{H_2}) at several axial (X) stations of the porous electrodes. The species concentrations are $C_{H_2} = 1.0$ (pure hydrogen) for the anode inlet and $C_{O_2} = 0.9$ and $C_{H_2O} = 0.1$ (humidified oxygen) for the cathode, respectively. The Reynolds number is fixed at $Re = 6$. At the axial station of $X = 0.4$, the pure hydrogen decreases its concentration from the inlet to the catalyst layer. As the flow moves downstream, C_{H_2} is gradually decreased due to the HOR in the catalyst layer. A similar trend is also observed for the oxygen concentration in the cathode. The lowest values of C_{H_2} and C_{O_2} at each axial station occur at the interfaces of the membrane and the catalyst layers, i.e., $Y = 0.45$ and 0.55, respectively. Fig. 5 further shows the distributions of the local minima of C_{H_2} and C_{O_2} along the axial direction (X). As the flow goes downstream, the distributions of the local minima of C_{H_2} and C_{O_2} start with a little decline, then drop sharply, and finally decrease mildly.

Fig. 6 compares the distributions of the fluid-phase temperature (θ_f) and the solid-phase temperature (θ_s) in the MEA under various $Bi/(Pr{\cdot}Re{\cdot}R_k)$. Again, no fluid-phase temperatures are shown in the membrane due to its impermeability. In the catalyst layers ($0.4 < Y < 0.45$, $0.55 < Y < 0.6$), the solid matrices and the fluids have the same temperatures. A local maximum temperature is clearly observed at about $Y = 0.57$, where significant heat is generated by the electrochemical reaction. In the diffusion layer, the fluid-phase temperature and solid-phase temperature separate from the interface of the catalyst layer and the gas diffusion layer due to the LTNE effect. The extent of temperature discrepancy between these two phases in the gas diffusion layer depends on $Bi/(Pr{\cdot}Re{\cdot}R_k)$ as well as the location. At the smallest value of $Bi/(Pr{\cdot}Re{\cdot}R_k) = 6.63 \times 10^{-3}$ (Fig. 6(a)), the fluid-phase temperature and the solid-phase temperature are rather different at the axial stations of $X = 0.8$ and 1.2. It is further seen that an increase in the value of $Bi/(Pr{\cdot}Re{\cdot}R_k)$ reduces the temperature discrepancy between the solid phase and the fluid phase. As the value of $Bi/(Pr{\cdot}Re{\cdot}R_k)$ increases to 6.63×10^{-3} (Fig. 6(d)), the fluid-phase temperature and the solid-phase temperature fall into a single curve almost. A great similarity in the temperature distribution between the solid phase and the fluid phase gives an indication that the thermal-fluid field in the porous electrode has become equilibrium locally.

Fig. 7(a and b) compare the temperature distributions in the MEA between two different values of $Bi/(Pr{\cdot}Re{\cdot}R_k)$ at three axial stations of $X = 0.4$, 0.8 and 1.2. As shown in Fig. 7(a) for the smaller value of $Bi/(Pr{\cdot}Re{\cdot}R_k)$ (6.63×10^{-3}), the fluid-

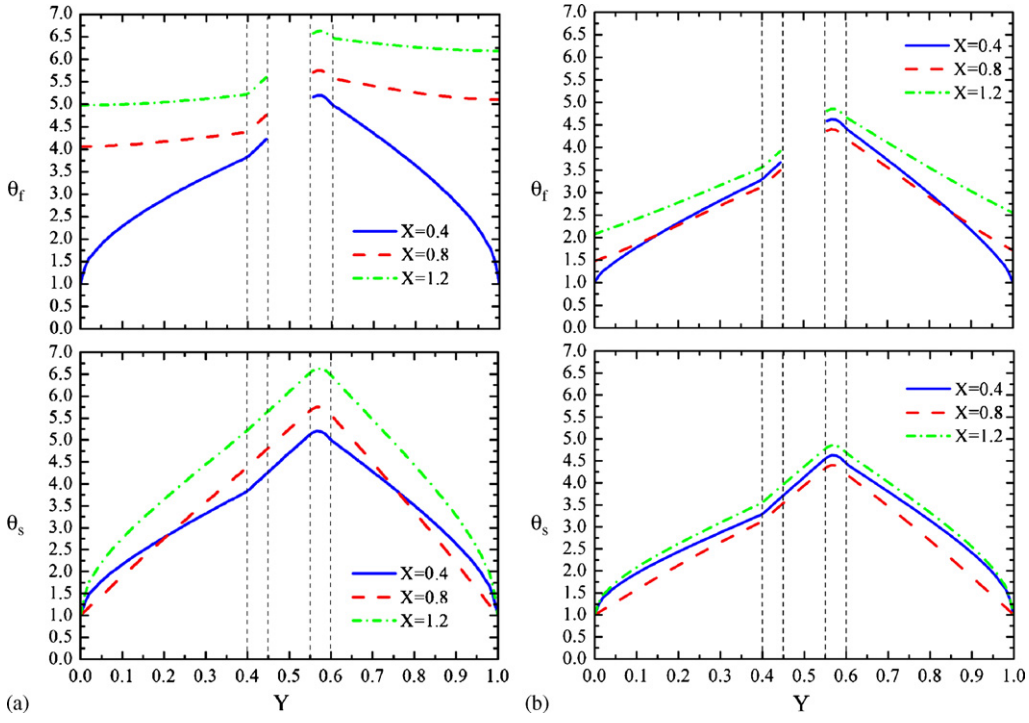

Fig. 7. Fluid-phase and solid-phase temperature distributions at several X stations in the MEA for (a) $Bi/(Pr{\cdot}Re{\cdot}R_k) = 6.63 \times 10^{-3}$, and (b) $Bi/(Pr{\cdot}Re{\cdot}R_k) = 6.63$.

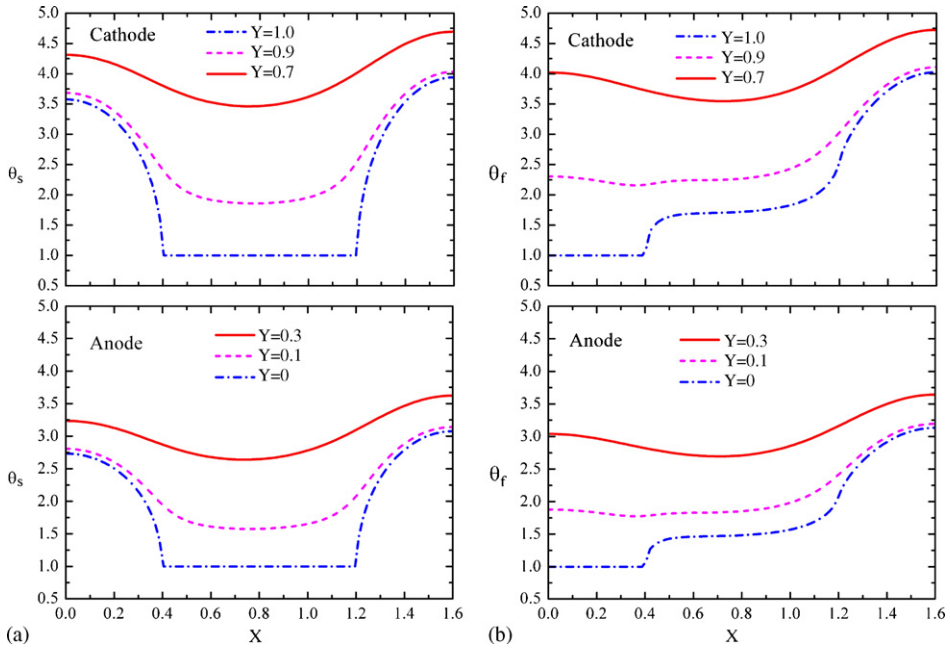

Fig. 8. Temperature distributions along X direction at several Y stations for $Bi/(Pr{\cdot}Re{\cdot}R_k) = 6.63$, (a) solid-phase temperature, and (b) fluid-phase temperature.

phase temperature increases monotonically downstream in both electrodes. The solid-phase temperature decreases downstream in the core region of the MEA but has the lowest value near the middle of the shoulder surfaces ($X = 0.8$). This is because the module middle has the shortest distance for heat conduction from the reaction surface to the heat sink (cold rib shoulder). When the value of $Bi/(Pr{\cdot}Re{\cdot}R_k)$ increases to 6.63 (Fig. 7(b)), both the fluid-phase temperature and the solid-phase temperature decrease. This is because an increase in the value of $Bi/(Pr{\cdot}Re{\cdot}R_k)$ enlarges the heat transfer gate between the solid phase and the fluid phase that enhances the cooling of the solid matrices by convection. That is the hot solid matrices can transfer a large portion of heat to the cold fluid via convection. In addition, the entire cross section of the module middle ($X = 0.8$) has the lowest values of solid-phase temperature as the value of $Bi/(Pr{\cdot}Re{\cdot}R_k)$ increases to 6.63.

Fig. 8(a and b) show the distributions of the solid-phase temperature and the fluid-phase temperature along the axial direction (X) at several elevations ($Y = 0$, 0.1, and 0.3 for the anode, and 0.7, 0.9 and 1.0 for the cathode), respectively. The Re and $Bi/(Pr{\cdot}Re{\cdot}R_k)$ are fixed at 6 and 6.63, respectively. As shown in this figure, the cathode has a higher solid-phase temperature than the anode at the corresponding location in respect to the module mid-plane ($Y = 0.5$). Again, it is because of a significant heat generation by the electrochemical reaction in the cathodic catalyst layer. The concave shape for the solid-phase temperature distributions reflects conduction-dominant transport phenomena in the solid phase heat transfer. In contrast, the fluid-phase temperature distribution near the shoulder surfaces increases downstream monotonously. At the elevation closed to catalyst layers, $Y = 0.3$, and 0.7, the distribution of fluid-phase temperature becomes concave. Fig. 9 further shows the temperature distributions along the two sides of the catalyst layers, i.e., $Y = 0.4$, 0.45, 0.55 and 0.6. The temperature distributions decrease first and then increases to a local maximum at the downstream end. A local minimum occurs at the module middle ($X = 0.8$). They are roughly symmetric about the local minimum at module middle ($Y = 0.8$) where faces the cold shoulder surfaces. Again, the concave of the temperature distributions gives an indication that the conduction dominates the thermal transport in the porous medium.

Fig. 10 shows the effect of Ec_{O_2} on the temperature distributions at the module middle (i.e., $X = 0.8$). The non-dimensional interfacial heat transfer coefficient is fixed at $Bi/(Pr{\cdot}Re{\cdot}R_k) = 6.63$. As given in Table 2, an increase in Ec_{O_2} means the increase in the overpotential heating during the electrochemical reaction. It is seen that, both the solid-phase temper-

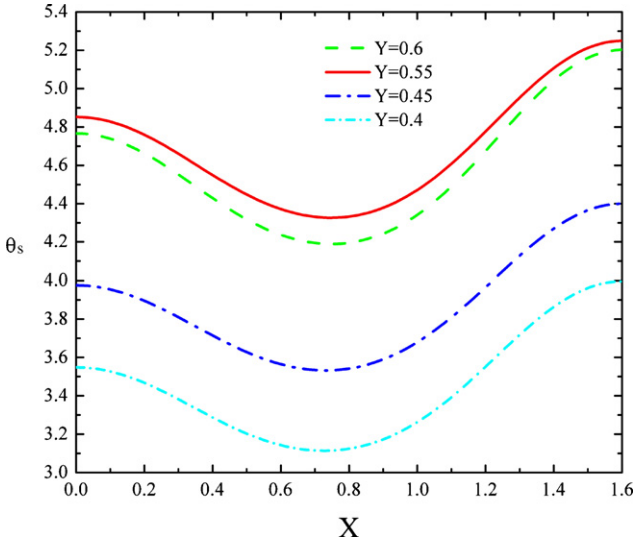

Fig. 9. Temperature distributions along the two sides of catalyst layers for $Bi/(Pr{\cdot}Re{\cdot}R_k) = 0.63$.

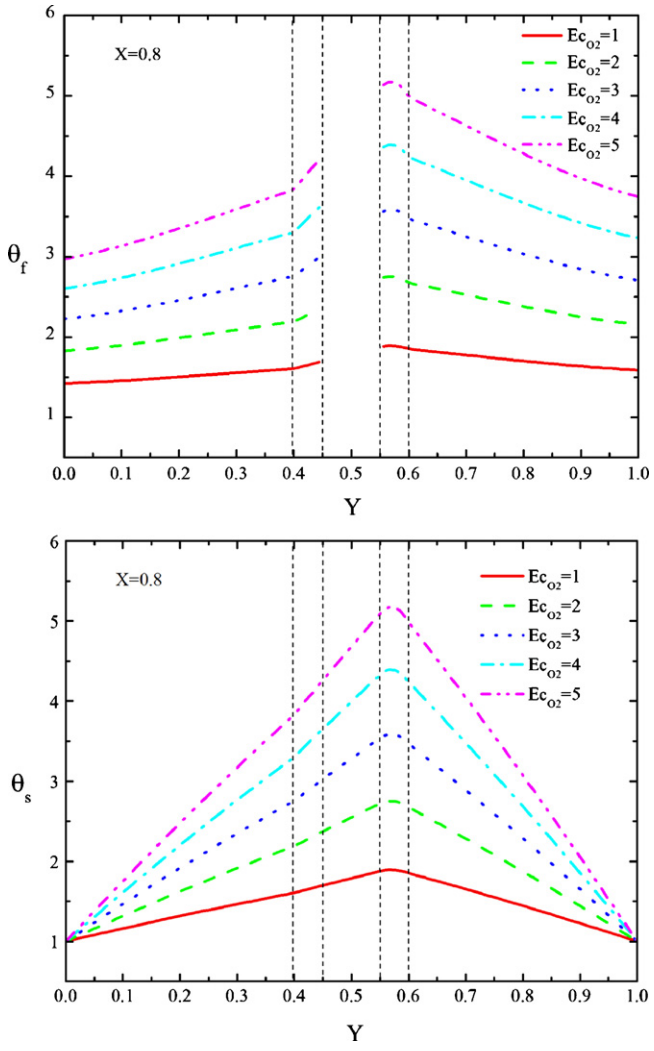

Fig. 10. Effect of overpotential heating on the temperature distributions inside the five-layer MEA, $Bi/(Pr{\cdot}Re{\cdot}R_k) = 6.63$.

ature and the fluid-phase temperature increase with increasing Ec_{O_2}. Since the heat dissipation in the cathodic catalyst layer is more than that in the anodic catalyst layer, both of the fluid-phase temperature and the solid-phase temperature are higher in the cathodic gas diffusion layer than those in the anodic gas diffusion layer.

4. Conclusions

A numerical model has been performed to simulate the thermal-fluid transport phenomena in a five-layer MEA of a PEM fuel cell, which is in contact with interdigitated gas distributors. Parametric studies include the flow Reynolds number (Re), non-dimensional heat transfer coefficient ($Bi/(Re{\cdot}Pr{\cdot}R_k)$), and electrochemical heat parameter (Ec_{O_2}). The unique of this model is the first implementation of the local thermal non-equilibrium model in the gas diffusion layers which allows for a more realistic variation of the thermal-fluid in the MEA of a PEM fuel cell. Results show that the local maximum temperature inside the MEA occurs at about the middle of the cathodic catalyst layer. In addition, an increase in the non-dimensional heat transfer coefficient $Bi/(Pr{\cdot}Re{\cdot}R_k)$ reduces the temperature difference between the solid matrices and the reactants in the gas diffusion layer. Moreover, both fluid-phase temperature and the solid-phase temperature decrease with increasing the non-dimensional heat transfer coefficient $Bi/(Re{\cdot}Pr{\cdot}R_k)$. It is further found that an increase in the overpotential heating parameter Ec_{O_2} increases the fluid and solid-phase temperatures. The present model has successfully predicted the heat/mass transfer mechanisms together with the thermal pathways in the MEA of PEM fuel cells. It would be beneficial for further accurate analyses of the fuel cell thermal performance by considering the thermal dependent physical properties inside the MEA.

Acknowledgment

This work was partly sponsored by the National Science Council of the Taiwan, ROC under contract No. NSC 92-2212-E-451-002.

References

[1] D.M. Bernardi, M.W. Verbrugge, AIChE J. 37 (1991) 1151–1162.
[2] T.E. Springer, T.A. Zawodzinski, S. Gottesfeld, J. Electrochem. Soc. 138 (1991) 2334–2342.
[3] T.V. Nguyen, R.E. White, J. Electrochem. Soc. 140 (1993) 2178–2186.
[4] V. Gurau, H. Liu, S. Kakac, AIChE J. 44 (1998) 2410–2421.
[5] J.S. Yi, T.V. Nguyen, J. Electrochem. Soc. 146 (1999) 38–45.
[6] S. Shimpalee, S. Dutta, Effect of humidity on PEM fuel cell performance Part-II numerical simulation, ASME paper, HTD346 (1999).
[7] J.J. Hwang, P.Y. Chen, Int. J. Heat Mass Transfer 49 (2006) 2315–2327.
[8] J.J. Hwang, ASME J. Heat Transfer 128 (2006) 434–443.
[9] C.H. Chao, J.J. Hwang, J. Power Sources 160 (2006) 1122–1130.
[10] M. Kaviany, Principles of Heat Transfer in Porous Media, second ed., Springer, Berlin, 1995.
[11] J.J. Hwang, G.J. Hwang, R.H. Yeh, C.H. Chao, ASME J. Heat Transfer 124 (2002) 120–129.
[12] B. Alazmi, K. Vafai, Int. J. Heat Mass Transfer 44 (2001) 1735–1749.
[13] B. Alazmi, K. Vafai, Int. J. Heat Mass Transfer 45 (2002) 3071–3087.
[14] F. Kuwahara, M. Shirota, A. Nakayama, Int. J. Heat Mass Transfer 44 (2001) 1153–1159.
[15] J.J. Hwang, C.K. Chen, R.F. Savinell, C.C. Liu, J. Wainright, J. Appl. Electrochem. 34 (2004) 217–224.
[16] M. Sahraoui, M. Kaviany, Int. J. Heat Mass Transfer 36 (1963) 1019–1033.
[17] H. Oldham, J. Myland, Fundamentals of Electrochemical Science, Academic Press Inc., 1994.
[18] J.J. Hwang, C.H. Chao, W.Y. Ho, C.L. Chang, D.Y. Wang, J. Power Sources 157 (2006) 85–97.
[19] J.J. Hwang, J. Electrochem. Soc. 153 (2006) A216–A224.
[20] J.J. Hwang, J. Electrochem. Soc. 153 (2006) A1584–A1590.
[21] J.J. Hwang, ASME J. Heat Transfer 120 (1998) 709–716.
[22] J.J. Hwang, C.K. Chen, D.Y. Lai, J. Power Sources 140 (2005) 235–242.
[23] J.J. Hwang, K.H. Lo, S.H. Wang, K.C. Tsay, Fuel cell dynamics and transport phenomena in a PEMFC, in: Proceedings of the 25th Conference on Theoretical and Applied Mechanics, Taichung, Taiwan, 2001, pp. 3611–3620 (in Chinese).